

A statistical study of magnetic field changes in the photosphere during solar flares using high-cadence vector magnetograms and their association with flare ribbons

RAHUL YADAV¹ AND M. D. KAZACHENKO^{1,2,3}

¹Laboratory for Atmospheric and Space Physics, University of Colorado, Boulder, CO 80303, USA; rahul.yadav@lasp.colorado.edu

²National Solar Observatory, 3665 Discovery Drive, 80303, Boulder, CO, USA

³Dept. of Astrophysical and Planetary Sciences, University of Colorado Boulder, 2000 Colorado Ave, 80305, Boulder, CO, USA

ABSTRACT

Abrupt and permanent photospheric magnetic field changes have been observed in many flares. It is believed that such changes are related to the reconfiguration of magnetic field lines, however, the real origin is still unclear. In this study we analyze 37 flares to understand the magnetic field vector changes in the photosphere using high-cadence (135 s) vector magnetograms obtained from the HMI/SDO. We also co-align these magnetogram sequences with flare ribbon images (1600 Å), obtained from the AIA/SDO, to understand how the field change is associated with the ribbon morphology. We find that the permanent change in the horizontal component lies near the polarity inversion line, whereas the vertical component pixels are less pronounced and distributed in small patches. We also find that the pixels exhibiting ultraviolet emission are not always associated with permanent field change. In 84% of 37 events the UV emission starts early by several minutes compared to the field change start time for the pixels showing both UV emission and permanent horizontal field change. The field change properties show no relation with the size of active regions, but are strongly related to the flare ribbon properties like ribbon magnetic flux and ribbon area. The permanent field change duration is strongly correlated with the GOES flaring duration, with an average value of 29% of total GOES flare time. Our analysis suggests that the change in photospheric magnetic field is caused by combination of two scenarios: contraction of flare loops driven by magnetic reconnection and coronal implosion.

Keywords: Sun: Magnetic fields – Sun: flares

1. INTRODUCTION

Solar flares are one of the most spectacular and energetic phenomena on the Sun. A typical flare is characterized by a rapid increase in light emission in a wide range of the electromagnetic spectrum, which affects the entire outer solar atmosphere, i.e., the photosphere, the chromosphere and the corona. Frequently, strong flares are accompanied by the coronal mass ejection (CME), releasing a large amount of radiation that may have severe space-weather impacts (Schrijver 2015). Therefore, understanding the real mechanism behind the explosive events like solar flares and CMEs has become one of the hot-topics in solar physics research (Benz 2008; Kazachenko et al. 2022a).

In the standard flare model, the fundamental mechanism of solar flares is believed to be magnetic reconnection or re-configuration of field lines in the corona, converting the magnetic energy into kinetic and thermal energies driving the acceleration of the particles into the lower solar atmosphere (Carmichael 1964; Sturrock

1966; Hirayama 1974; Kopp & Pneuman 1976). The deposition of energy gives rise to intense brightening and emission of hard and soft X-rays in the lower solar atmosphere. The appearance of bright structures in the chromosphere or transition region are normally referred to as flare ribbons. These ribbons indicate footpoints of reconnected field lines. Their morphology is frequently utilized to trace the evolution of coronal magnetic energy release (Longcope et al. 2007; Kazachenko et al. 2012; Qiu et al. 2017). As the coronal magnetic field lines are rooted in the photosphere, the investigation of magnetic field topology and the evolution of field lines from lower solar atmosphere up to the corona is required to understand different aspects of a flare (Hudson 2011).

Flare observations have demonstrated that an intense flare can distort the structure of active regions (ARs), rapidly rotate sunspots in the photosphere (Wang et al. 2014; Liu et al. 2016; Xu et al. 2018) and can contract and oscillate the coronal loops (Russell et al. 2015; Wang et al. 2016). Additionally, the availability of

high-cadence photospheric vector magnetograms from ground-based and space-based telescopes, such as *Solar Dynamics Observatory* (SDO; Pesnell et al. 2012), have provided us evidence of rapid and permanent changes in the longitudinal and transverse magnetic fields associated with solar flares in the photosphere (Sudol & Harvey 2005; Petrie & Sudol 2010; Wang et al. 2012; Gosain 2012; Sun et al. 2017; Castellanos Durán et al. 2018; Petrie 2019; Liu et al. 2022). Recently, the magnetic field changes in the chromosphere, in addition to the photosphere, have also been reported from flare observations performed at ground-based observatories (Kleint 2017; Yadav et al. 2021).

Observational evidence of increase in the horizontal component of magnetic field in the photosphere and the contraction of coronal loops during a flare is generally interpreted with the conjecture proposed by Hudson (2000), also known as ‘coronal implosion’. It states that during a transient event such as a flare or a CME, in a low plasma- β atmosphere with negligible gravity, the coronal field lines must contract in such a way as to reduce the magnetic energy, $E_{mag} = \int_V B^2/8\pi dV$. The release of the free magnetic energy should be accompanied by decrease in the magnetic pressure and volume, which can lead to loop contraction at the flare sites (Hudson et al. 2008; Fisher et al. 2012). The loop contraction during flares has been noticed in numerous observations (e.g. Liu et al. 2009; Simões et al. 2013). Such coronal magnetic implosion or loop contractions could increase the horizontal component of the magnetic field in the photosphere near the polarity inversion line (PIL).

Numerical studies have also been performed by various authors to understand the mechanism behind the loop contractions and related field change. Li et al. 2011 analyzed flare-associated changes of the magnetic field in the observation and simulation. They found that both observation and simulation show an enhancement in the horizontal magnetic field near the flaring PIL after the flare. They argued that these changes are natural consequences of the lift-off of the pre-existing coronal flux rope, and the subsequent implosion of the magnetic field with the inward collapsing of the post-reconnection loops above the PIL, consistent with the prediction by Hudson et al. 2008. In a 3D magnetohydrodynamic model of an erupting magnetic flux rope, Zuccarello et al. 2017 found that vortices developed on both sides of the expanding flux-rope footpoints during a flare eruption could cause the loop contraction. Within the framework of ideal magnetohydrodynamics Sarkar et al. (2017) found that the dynamics of loop implosion is also sensitive to the velocity disturbance gener-

ated close to the reconnection site. Recently, Barczynski et al. (2019) performed a generic 3D magnetohydrodynamics simulation of an eruptive flare to understand the mechanism behind the field change. They concluded that the increase in the photospheric horizontal magnetic fields result from the reconnection-driven contraction of sheared flare loops. Their conclusion contradicts previous interpretations that were based on momentum conservation between the upward-moving CME and the underlying photosphere, or based on the implosion conjecture alone.

During the last decades, the photospheric magnetograms available from various space-based instruments have improved our understanding of the photospheric changes associated with flares. However, most of the previous studies were performed with a low cadence or focused more on the longitudinal changes. For example, vector magnetograms obtained from the Helioseismic and Magnetic Imager (HMI/SDO; Scherrer et al. 2012) have a cadence of 12 minutes, which is not sufficient to temporarily resolve fast changes that normally occur during a flare.

In this study, we present statistical analysis of flares to understand their magnetic imprints in the photosphere using high-cadence (135 s) vector magnetograms obtained from HMI/SDO. We aim to clarify how the characteristics of photospheric field changes are related to ultraviolet (UV) emissions and ribbon morphology, which are the footpoints of reconnected field lines.

The rest of the paper is structured as follows. In Section 2, we describe our data set and methods employed to characterize the field changes. We present our results in Section 3. We then discuss them in Section 4. Finally, in Section 5, we summarize our conclusions.

2. DATA AND METHODS

In this study we selected 37 flaring events including 8 X-, 27 M-, and 2 C-class flares in 31 active regions (AR) listed in Table 1. These events are taken from the FlareMagDB¹ catalog created by Kazachenko et al. (2022b). As shown in the Figure 1 selected events are distributed within 45° from the disk center and occurred from August 2010 to November 2015 (see Table 1). For each event we used the high-cadence (135 s) full-disk vector magnetograms obtained from the HMI (Scherrer et al. 2012) onboard SDO (Pesnell et al. 2012). The HMI samples the spectral region around the Fe I 6173.3 Å absorption line at six wavelength points with a bandwidth of 76 mÅ and records full set of Stokes parameters (I,

¹ <http://solarmuri.ssl.berkeley.edu/~kazachenko/FlareMagDB/>

Table 1. List of 37 flares. For each event we show the following flare properties: NOAA AR number, location on the solar disk, total cumulative ribbon area (S_{rbn}), total AR area (S_{AR}), total unsigned magnetic flux in ribbons (Φ_{rbn}) and in the AR (Φ_{AR}), GOES flare duration (τ_{GOES}), and ribbon distance (d_{rbn}). The Area is expressed in millionths of the solar hemisphere (MSH), which is equivalent to $3 \times 10^6 \text{ km}^2$.

Event no.	Flare start time (UT)	NOAA AR no.	Flare Class	Location on Disk	S_{rbn} (MSH)	S_{AR} (MSH)	$ \Phi_{\text{rbn}} $ (10^{21} Mx)	$ \Phi_{\text{AR}} $ (10^{21} Mx)	τ_{GOES} (min.)	d_{rbn} (Mm)
1	2010-08-07T17:55	11093	M1.0	N12E31	317	2857	4.8	30.3	51.2	62.5
2	2011-02-15T01:43	11158	X2.2	S20W10	512	1863	11.6	30.7	32.8	27.1
3	2011-08-03T13:17	11261	M6.0	N16W30	370	3495	7.6	43.4	52.4	51.0
4	2011-09-06T22:11	11283	X2.1	N14W18	436	2436	5.9	26.4	27.6	9.6
5	2011-10-02T00:37	11305	M3.9	N12W26	178	1387	2.4	16.7	21.2	15.6
6	2011-11-15T12:29	11346	M1.9	S18E26	215	8098	3.5	52.9	19.6	14.4
7	2011-12-27T04:11	11386	C8.9	S17E23	139	4366	2.0	40.6	19.2	26.1
8	2012-01-23T03:37	11402	M8.7	N33W21	892	8002	17.0	94.5	55.6	51.8
9	2012-03-07T00:01	11429	X5.4	N18E31	1173	6152	30.4	77.1	37.6	51.3
10	2012-03-09T03:21	11429	M6.3	N15W03	768	3920	14.4	57.1	55.6	30.8
11	2012-03-10T17:15	11429	M8.4	N17W24	904	4412	16.9	61.9	74.4	43.6
12	2012-03-14T15:07	11432	M2.8	N14E01	234	1933	3.1	18.6	27.6	18.8
13	2012-07-12T15:37	11520	X1.4	S13W03	428	6335	8.6	85.9	58.4	53.0
14	2012-11-21T06:45	11618	M1.4	N08W00	194	2104	3.4	26.0	22.4	27.6
15	2013-04-11T06:55	11719	M6.5	N07E13	324	2959	4.5	29.2	33.2	17.4
16	2013-05-16T21:35	11748	M1.3	N11E37	222	5779	3.8	43.4	26.8	33.5
17	2013-05-31T19:51	11760	M1.0	N12E37	151	6568	2.1	36.0	13.6	9.7
18	2013-08-17T18:49	11818	M1.4	S07W32	313	4395	6.1	50.2	58.4	33.4
19	2013-12-28T17:53	11936	C9.3	S16E07	105	2330	1.4	24.5	14.4	11.4
20	2014-01-07T18:03	11944	X1.2	S12W08	792	5075	11.6	73.4	53.6	102.0
21	2014-01-31T15:31	11968	M1.1	N09E29	317	7638	3.4	63.2	20.8	51.0
22	2014-02-01T07:13	11967	M3.0	S14E17	222	5993	5.5	92.7	21.6	65.9
23	2014-02-12T03:51	11974	M3.7	S12W11	408	3052	6.7	37.8	45.6	63.3
24	2014-03-20T03:41	12010	M1.7	S15E27	228	5029	3.4	49.9	25.6	46.3
25	2014-08-01T17:55	12127	M1.5	S09E08	409	3809	5.2	38.6	52.4	46.5
26	2014-08-25T14:45	12146	M2.0	N06W39	221	3870	4.5	42.3	44.8	14.4
27	2014-08-25T20:05	12146	M3.9	N07W43	253	4494	6.0	45.4	22.8	14.8
28	2014-09-08T23:11	12158	M4.5	N16E26	309	3166	8.4	42.6	58.8	36.0
29	2014-09-10T17:21	12158	X1.6	N11E05	702	2374	12.2	30.0	58.4	38.7
30	2014-09-28T02:39	12173	M5.1	S13W23	361	5890	7.0	79.9	39.2	53.2
31	2014-10-22T14:01	12192	X1.6	S14E13	811	9632	17.7	155.9	47.6	70.9
32	2014-12-17T00:57	12242	M1.5	S20E08	151	5538	2.8	67.8	22.4	50.0
33	2014-12-17T04:25	12242	M8.7	S18E08	379	5639	8.5	69.7	54.4	32.0
34	2014-12-18T21:41	12241	M6.9	S11E10	461	3622	9.3	48.6	43.2	15.6
35	2014-12-20T00:11	12242	X1.8	S19W29	1289	7974	26.5	113.6	43.2	53.6
36	2015-11-04T13:31	12443	M3.7	N06W10	535	3364	6.9	39.0	41.2	45.7
37	2015-11-09T12:49	12449	M3.9	S12E33	476	7828	8.4	55.3	38.4	25.2

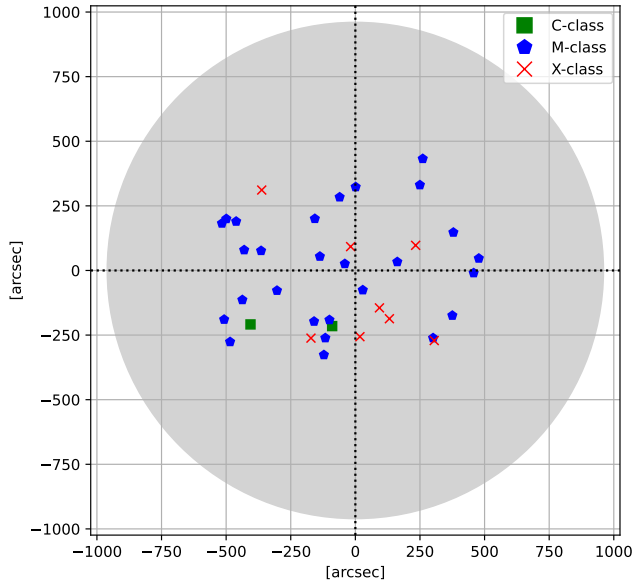


Figure 1. Location of selected flare events on the artificial solar disk. Green square, blue pentagon, and red cross symbols indicate the position of C-, M-, and X-class solar flares on the solar disk, respectively.

Q, U, V) in 135 s with a pixel size of $0.5''$. The post-processing and data acquisition of 135 s cadence vector magnetograms are described in Sun et al. (2017). The full-disk vector magnetogram² is retrieved by inverting full set of Stokes parameters using the Milne-Eddington inversion approach (Borrero et al. 2011). To resolve the azimuth ambiguity we employed the `hmi_disambig.pro` routine of the HMI SolarSoft package. After this 180-ambiguity correction, we transformed the magnetic field vector inferred in the line-of-sight frame to the solar local reference frame using the transformation matrix given by Gary & Hagyard (1990).

Sun et al. (2017) have carried out a comparison between pairs of 135 and 720 s full disk vector magnetograms retrieved from HMI. They found that the 135 and 720 s data agree well in the strong-field regions ($B > 300$ G). However, in comparison to 720 s, the 135 s data have higher noise due to shorter integration time.

For each flaring event, in addition to HMI vector magnetograms, we also used a sequence of 1600 \AA images, obtained from the Atmospheric Imaging Assembly (AIA; Lemen et al. 2012) onboard SDO, at the cadence of 24 s with a pixel size of $0.6''$ covering full evolution of flare ribbons. These AIA 1600 \AA images are used to trace the morphology of flare ribbons. Then we use the

² http://jsoc.stanford.edu/ajax/lookdata.html?ds=hmi.B_135s

`aia_prep.pro` routine of the SolarSoft package to align the AIA images sequences with the HMI vector magnetograms. For further analysis we define the region of interest centered on the active region and covering the entire flare ribbon area. The final co-aligned AIA and HMI data consists of a cube of $480'' \times 480''$ field-of-view with a $0.6''$ pixel scale.

To characterize and study the evolution of the field changes, we selected a 2-hour interval around the flaring time, one hour before and after the GOES flare peak time. The flare start, peak and end time are identified using *Geostationary Operational Environmental Satellite* (GOES) $1 - 8 \text{ \AA}$ X-ray flux. The magnetic field map sequence of 2 hours with a cadence of 135 s is sufficient to capture the permanent field changes in all events, except one case, where the flaring duration was around 75 minutes (event no. 11 in Table 1). For this event we selected a 3-hour interval (one and half hours on either side of the flare peak time).

2.1. Desaturation of AIA 1600 \AA images

We used SDO/AIA 1600 \AA images and HMI magnetograms to compare ultraviolet (UV) emissions from the chromosphere to the magnetic field changes in the photosphere during 37 selected flares. The energy released during flares in the chromosphere and the transition region give rise to emissions in the flare ribbons. If the heating caused by a flare is sufficiently strong then the AIA 1600 \AA pixels located on the flare ribbon get saturated due to the diffraction patterns from the EUV-telescope entrance filter and CCD saturation.

To correct the saturated intensities of pixels we employed the method given by Kazachenko et al. (2017). In this approach, we first identify the pixels above a threshold intensity ($5000 \text{ counts s}^{-1}$) and neighboring 2 and 10 pixels in the x - and y - directions, respectively. In the next step, we replace all selected pixel intensities with the value obtained from linear interpolation in time between the previous and the following image sequences when the pixels are unsaturated. More details regarding this method are given in Kazachenko et al. (2017). For further analysis we used the saturation corrected images.

2.2. Determination of permanent magnetic field changes

To determine and characterize the permanent field changes in the selected field of view, we fitted the co-aligned time sequences of horizontal ($B_h = \sqrt{B_x^2 + B_y^2}$) and vertical (B_z) components of magnetic field in each pixel with a step-like function (Sudol & Harvey 2005),

$$B_i(t) = a + bt + c \left\{ 1 + \frac{2}{\pi} \tan^{-1} [n(t - T_m)] \right\}, \quad (1)$$

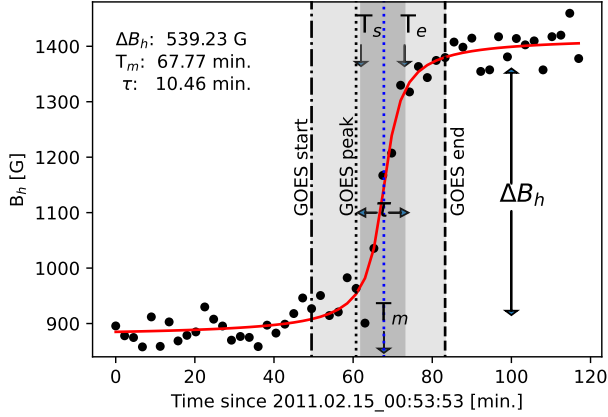


Figure 2. Demonstration of parameters that we used to describe the magnetic field changes in a single pixel (see Equation 1). Temporal evolution of the horizontal magnetic field during a X2.2 flare for a single pixel is indicated by black circles, whereas the red line is the best fit of Equation 1. The field change start (T_s) and end (T_e) times are indicated by black arrows. The dark gray shaded area indicates field change duration (τ), whereas the total light and dark gray shaded area refer to the GOES X-ray flaring duration. ΔB_h refers to the measure of the field change. A dotted blue line indicates the mid-time of field change (T_m). Dotted dashed, dotted, and dashed black lines indicate GOES flare start, peak and end time, respectively.

where $a + bt$ describes a linear evolution of the background field with time t , c represents the half amplitude of the step, n is the inverse of the time interval controlling the slope of the step, and T_m is the time corresponding to the midpoint of the step.

The temporal evolution of each pixel is then fitted by varying the free parameters: a, b, c, n , and T_m . To fit the step-like function we used the Levenberg-Marquardt method of nonlinear least-squares minimization. The best fitted parameters are then used to characterize the field changes and to create maps of fitted parameters: ΔB_i , τ , $\Delta \dot{B}$, T_m , T_s , and T_e . The $\Delta B_i = 2c$ is a measure of the change in the magnetic field (in Gauss). The $\tau = \pi n^{-1}$ corresponds to the period of time over which the magnetic field change occurs or field change duration (in minutes). The $\Delta \dot{B} = \Delta B/\tau$ corresponds to the rate of change in the magnetic field (in G/min). The T_m is the middle time of the field change. The field change start and end time are estimated as $T_s = T_m - \tau/2$ and $T_e = T_m + \tau/2$, respectively. These derived parameters are demonstrated in Figure 2.

2.3. Criteria to characterize the magnetic field changes

In our data set, we find that there are different types of field evolution in both B_h and B_z , which cannot be entirely described by Equation 1. While some changes

are related to flare, some of them may be related to flux emergence or cancellation that could lead to non-linear background evolution of the magnetic field. In this study, we do not investigate the role of flux emergence or cancellation, but focus only on the permanent magnetic field changes in the selected events. To identify the correct characteristics and permanent change in the magnetic field, we apply the following criteria to each pixel fitted using the Eq. 1.

1. The pixels should reside in the flare ribbon area or the field strength of the pixels should be greater than 300 G: $|B| > 300$ G
2. ΔB value should be greater than 100 G and the maximum ΔB value should be less than 800 G. We impose these limits to avoid pixels having value less than the uncertainty of B or having a strong background evolution due to moving magnetic features near the AR (Hagenaar & Shine 2005).
3. The field change start and end time should lie within the flaring duration given by GOES X-ray flux. In some pixels we find that the field change begins before the flare start time and the field change ends after the flare end time. Such pixels (< 1%) are not included in the analysis as they may not be related to flares. Moreover, the mid time of field change, T_m , should lie within the GOES flare start and end times. Pixels with T_m value beyond the flaring duration are excluded.
4. The change duration, τ , should be greater than the cadence of HMI vector magnetograms (135 s), even-though there are a small number of pixels exhibiting τ less than 135s.

The pixels satisfying above conditions and having the best χ^2 values (< 3) obtained from Equation 1 are then used to estimate the following parameters in the selected region: ΔB_i , τ , $\Delta \dot{B}$, T_m , T_s , and T_e . As an example, the parameters retrieved after fitting a single pixel, using Eq. 1, are illustrated in Figure 2.

Additionally, for each event we also defined the following AR and flare properties (see Table 1): the total AR area (S_{AR}), calculated as the area of the pixels having intensity less than 85% of the quiet-Sun intensity from limb-darkening corrected continuum images (Pettauer & Brandt 1997); the total cumulative ribbon area (S_{rbn}), total unsigned magnetic flux in the AR (Φ_{AR}) and the total flux in the cumulative ribbon area (Φ_{rbn}) are estimated following the approach given by Kazachenko et al. (2017); the GOES flare duration (τ_{GOES}) is defined as the time difference between the GOES flare start and

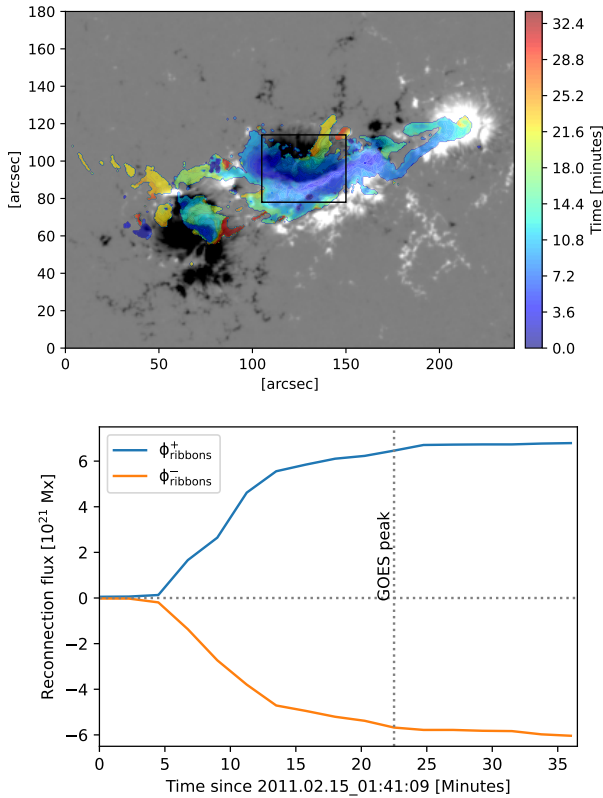


Figure 3. Evolution of flare ribbons during an X2.2 flare on February 15 2011. *Top panel:* Spatial locations and evolution of ribbons color-coded in time. The vertical component of the magnetic field (B_z) is shown as background, where black and white colors indicate negative and positive polarity (saturated at ± 800 G), respectively. The black box shows the FOV for Figure 4. *Bottom panel:* Time profiles of the total reconnection flux integrated in the positive and negative polarities, respectively. The vertical dotted line indicates the GOES X-ray peak time.

end times for each event; the ribbon distance (d_{rbn}) is estimated as the separation between the two magnetic flux weighted centroids of the ribbons in the positive and negative polarities (see Figure 11 in appendix).

3. RESULTS

In the following sections we first describe the characteristics of field changes and their association with UV emission for an example X2.2 flare observed on February 15, 2011. We then summarize statistical results and the correlations between different variables derived from the step-like function for 37 events.

3.1. Case study: Analysis of field changes in an X2.2 flare on February 15 2011

As an example, we first analyze and derive the characteristics of field changes in X2.2-class flare (SOL2011-

02-15T01:56). The temporal evolution of flare ribbons associated with this flare is shown in Figure 3, where the violet and red colors correspond to early and late stages of the flare, respectively. Similar to Kazachenko et al. (2017), the total unsigned ribbon area is estimated using the cumulative ribbon pixels. The evolution of the magnetic fluxes swept up by ribbons in positive (Φ_{ribbons}^+) and negative (Φ_{ribbons}^-) polarities, shown in the bottom panel of Figure 3, are determined using the Equation 3 given in Kazachenko et al. (2017).

3.1.1. Magnetic field changes during an X2.2 flare

Figure 4 shows a map of parameters describing field change characteristics during an X2.2-class flare (SOL2011-02-15T01:56): field change magnitude ΔB_h , field change start time T_s and duration τ obtained from the step-like function (see Equation 1) for B_h (Figure 4; a, b, c) and B_z (Figure 4; d, e, f) components of magnetic field. Additionally, panel g shows the temporal evolution of chromospheric ribbons, where color corresponds to initial ribbon brightening in each pixels. As described in Section 2.2, we fitted the temporal evolution of B_h and B_z , separately. In total 2676 out of 6195 pixels satisfied our criteria (see Sec. 2.3) for B_h . As demonstrated in the maps, pixels showing ΔB_h and ΔB_z are located in the umbra, penumbra, and near the PIL of the AR. However, the majority of pixels showing ΔB_h are located near the PIL, which is in agreement with previous studies (e.g., Sun et al. 2017; Liu et al. 2022). Figure 4 also demonstrates that, in comparison to ΔB_h , ΔB_z is less pronounced and is distributed in small patches of pixels over the whole AR. Panels b and c display how the field change start time and field change duration are distributed over the AR. We find that the pixels located close to the PIL exhibit fast and early permanent change in B_h , whereas the pixels located away from the PIL have slower and later-occurring permanent field changes (i.e. larger T_s and τ). For the B_z component, ΔB_z , T_s and τ are sparsely distributed over the AR without a clear pattern.

In Figure 5 we demonstrate how the B_h , τ , T_m , T_s , and temporal/spatial evolution of ribbons change along a solid line shown in Figure 4. The pixels located near the PIL show strong ΔB_h value, but the magnitude decreases for the pixels located away from the PIL. Moreover, T_m and T_s parameters increase gradually as we go further away from the PIL. Pixels located near the PIL exhibit fast and early change relative to the GOES peak time, whereas the pixels located away from the PIL have longer τ , T_s , and T_m values. Panel b also shows that ribbons appear earlier than T_m and T_s before the GOES peak time. In summary, Figures 4 and 5 suggest that

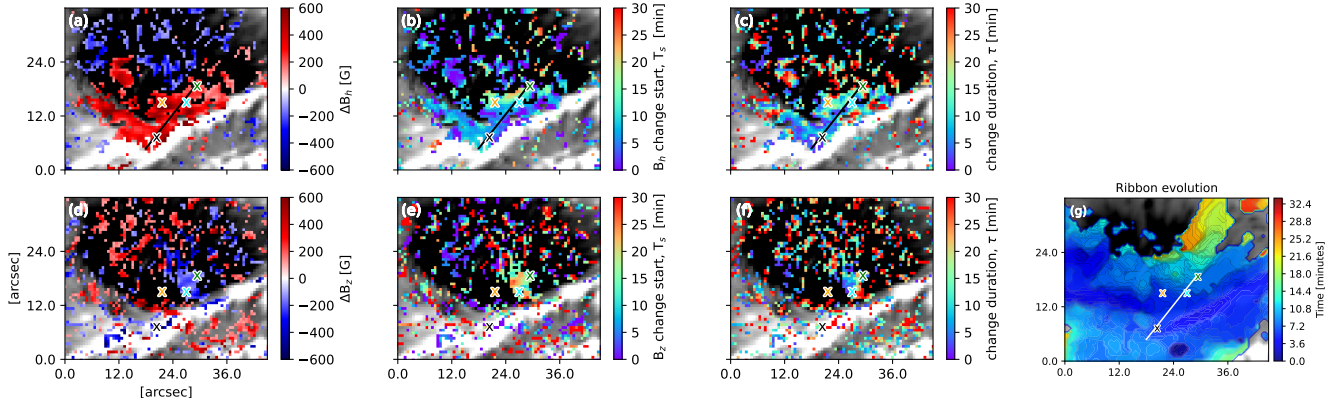


Figure 4. Characteristics of the field changes derived from the step-like function during an X2.2 flare on February 15 2011 starting 01:56UT. *Top panels:* The distribution of magnetic field change (a; ΔB_h), field change start time (b; T_s), and field change duration (c; τ) for the B_h component. *Bottom panels* (d, e, f): Same as top panels but for the B_z component. The zero value in the T_s is the flare start time. Right panel (g) shows the temporal evolution of ribbons, where color shows the initial ribbon brightening time in each pixel. Spatial distribution of parameters along a black (white) line is shown in Figure 5. The temporal evolution of pixels marked by cross symbols are shown in Figure 6. The background image in all panels shows the B_z component of the magnetic field (saturated at ± 800 G), where white and black refers to the positive and negative polarities, respectively.

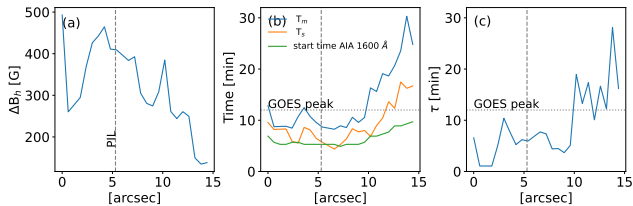


Figure 5. Field change properties along a solid line shown in Figure 4. (a) Change in ΔB_h ; (b) mid-time of field change (T_m ; blue line), field changes start time (T_s ; orange line), and the brightening start time of ribbons (AIA 1600 Å; green line); (c) field change duration τ . The zero value in time (panel b) is the flare start time. A dotted horizontal and dashed vertical lines are the GOES flare peak time and the PIL location, respectively.

pixels located near the PIL exhibit early field changes and shorter change durations with larger magnitudes of ΔB_h compared to pixels located $\sim 10''$ from the PIL, which is in line with previous studies (Sun et al. 2017; Castellanos Durán et al. 2018; Liu et al. 2022).

In Figure 6, we highlight temporal evolution of four pixels, marked with colored cross symbols in Figure 4. For these four pixels we show temporal evolution of horizontal and vertical components of magnetic field, AIA 1600 Å intensity and vertical current density ($J_z = \mu_0^{-1}(\nabla \times B)$). The temporal evolution of $B_{h,z}$ shows significant evidence of field change. Some of the pixels show clear and fast ($\tau = 3.23$ min) permanent step-like change in B_h , whereas some pixels exhibit slower ($\tau = 19.47$ min) and larger ΔB_h (~ 647 G) change. In some pixels we noticed permanent step-like change in

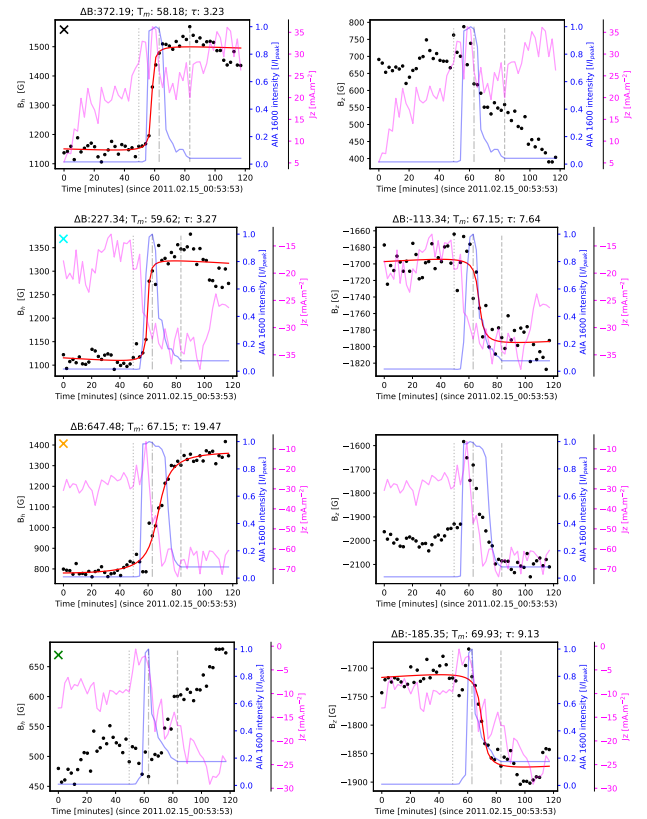


Figure 6. Temporal evolution of B_z , B_h , J_z , and AIA 1600 Å intensity in four pixels highlighted by colored cross symbols in Figure 4. The black dot refers to the observed B_z , B_h values, whereas the best fitted profiles obtained from the step-like function are shown in red solid line. The vertical dotted, dashed-dotted, and dashed line indicates the GOES flare start, peak and end time, respectively.

both the B_h and B_z components of the magnetic field, although generally ΔB_h is stronger than ΔB_z . Moreover, we also found pixels exhibiting no clear step-like change in the B_h , but a clear step-like change pattern in B_z .

There are some cases where the magnetic field vector retrieved from the inversions is not reliable as the Stokes observations are impacted by flare. As an example, the pixel marked by orange colored cross symbol (see Figure 6) shows sudden abrupt/transient change in B_z (~ 400 G) near flare peak time (see black dots), however, the change before and after the flare is below 100 G. Such pixels are excluded from our analysis, but need more attention to understand the flare-related artifact in the Stokes profile, which is out of the scope of this work. In a X2.2-class flare, [Maurya et al. \(2012\)](#) reported that the polarity reversal is a consequence of the line profile change. They concluded that the magnetic transient is not intrinsic to the Sun, but is an artifact in magnetic measurements due to the change of line profile.

In addition to the temporal evolution of B_h and B_z , Figure 6 also shows co-temporal and co-spatial J_z and the AIA 1600 Å intensity for the selected pixels. To investigate the relation between J_z and B_h , we measure the change in J_z at T_s and T_e , $\Delta J_z = J_z(T_e) - J_z(T_s)$, for all pixels showing step-like change. From the comparison of ΔJ_z and ΔB_h we find that they are not related to each other. As illustrated in Figure 6, J_z show some remarkable step-like behavior near the PIL, but these patterns are not consistent with the permanent field change (e.g., top panels of Figure 6). From analysis of six major flares [Petrie \(2012\)](#) also reported that changes in J_z show no consistent patterns.

3.1.2. Relationship between the AIA 1600 Å emission and the magnetic field changes during an X2.2 flare

For analyzed X2.2 flare on February 15 2011, the AIA 1600 Å intensity change generally starts after the GOES flare start time, peaks at the GOES flare peak time and then decreases gradually (see Figure 6, blue lines). We also analyzed how the selected pixels exhibiting permanent field change are related to UV emission (AIA 1600 Å). We find that some pixels exhibiting UV brightness show permanent B_h change, but not all brightening pixels are accompanied by field change, which is in line with [Johnstone et al. \(2012\)](#). For the X2.2 flare out of 2676 pixels showing permanent field change, only 41% pixels accompanied the UV brightening.

In Figure 7 we show relation between the start time of UV brightening and permanent field change in B_h . To determine the start time of UV brightening we employed an intensity threshold, which is 3 times larger than the

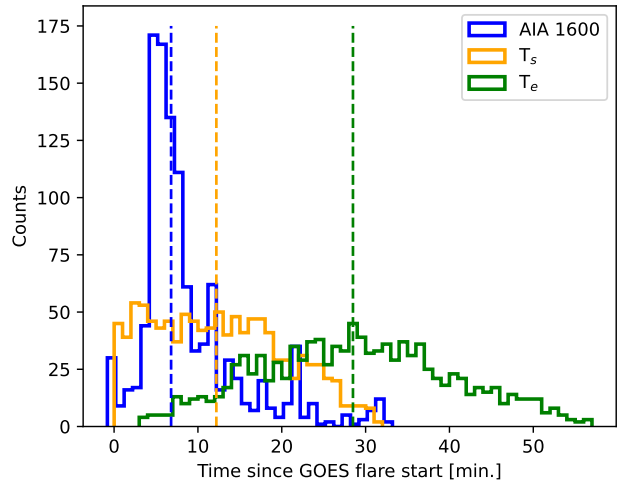


Figure 7. Histograms of AIA 1600 intensity change start time, B_h change start (T_s) and end time (T_e) for the SOL2011-02-15T01:56 X2.2-class flare. The vertical dashed lines denote the median values of AIA 1600 Å intensity change time (blue), B_h change start (orange) and end time (green).

median value of AIA 1600 Å quiet-Sun intensity. We find that the majority of pixels exhibiting AIA 1600 Å intensity change start after the GOES flare start time. However, 2.6% pixels out of 1099 show intensity rise before the GOES flare start time. These early UV brightenings can be caused by sequential chromospheric brightenings that could be caused by enhanced particle beams from the corona ([Balasubramaniam et al. 2005](#)). In most of the pixels the UV emission starts early compared to the field change start time. The median values of AIA intensity start time, T_s , and T_e are 6.8, 12.2, and 28.5 minutes, respectively. The median time delay between the start of the UV emission and the start of the change in the magnetic field is 5.4 minutes.

We applied the same procedure to remaining events to find out the delay in magnetic field changes associated with flare ribbons. In $\sim 85\%$ events, we find that the UV emission starts early compared to field change start time, T_s . For these events, the median value of field change delay is 4.4 minutes and the maximum delay is around 19 minutes. On the other hand $\sim 15\%$ events showing early T_s relative to AIA intensity start time could be due to irregular small-scale brightening, which is not detected by our intensity threshold.

3.2. Statistical properties of field changes in 37 flares

In this section we present the statistical analysis of all events shown in Table 1. For consistency, we employed the same procedure, as described above to all events. (see Section 2.2). Here we discuss the sta-

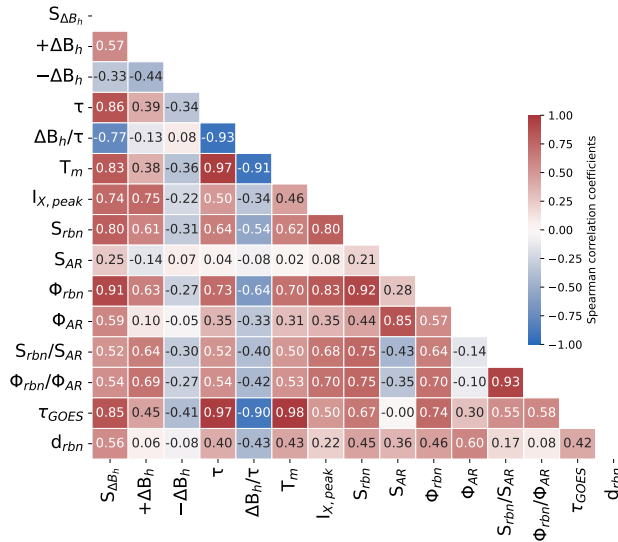


Figure 8. Correlation matrix showing Spearman correlation coefficients between different properties of B_h for 37 flares. The correlations are performed among: Total area showing step-like change ($S_{\Delta B_h}$), positive and negative change in B_h , change duration (τ), field change rate ($\Delta B_h/\tau$), mid-time of change (T_m), GOES X-ray peak flux ($I_{X,peak}$), total area of ribbons ($S_{r_{bn}}$), active region area (S_{AR}), total magnetic flux in ribbons ($\Phi_{r_{bn}}$), total magnetic flux in AR (Φ_{AR}), ratio of ribbon to active region area ($S_{r_{bn}}/S_{AR}$), ratio of ribbon flux to active region flux ($\Phi_{r_{bn}}/\Phi_{AR}$), GOES flare duration (τ_{GOES}), and ribbon distance ($d_{r_{bn}}$).

tistical properties of physical parameters derived after fitting the time series of B_h for each pixel with the step-like function (Equation 1; see Table 2 and Figure 12 in appendix). Additionally, we also analyzed the relationship between field change properties and other AR and flare parameters including the GOES X-ray peak flux intensity ($I_{x,peak}$), S_{AR} , $S_{r_{bn}}$, Φ_{AR} , $\Phi_{r_{bn}}$, τ_{GOES} , and $d_{r_{bn}}$.

Figure 8 shows the Spearman correlation coefficient (cc) between different parameters derived from all flaring events. The strength of correlation is color coded. To describe the qualitative strength of the correlation we adopted the following guideline given by Kazachenko et al. (2017): $cc \in [0.2, 0.39]$ —weak, $cc \in [0.4, 0.59]$ —moderate, $cc \in [0.6, 0.79]$ —strong, and $cc \in [0.8, 1.0]$ —very strong.

Figure 9 shows examples of scatter plots between derived parameters from Figure 8. We find that the median ΔB_h value for all events ranges from 100 G to 300 G (Figure 9b). We also find that the total area showing permanent change in B_h and the magnitude of ΔB_h are strongly related with the GOES X-ray flux (Figure 9a and b). This suggests that stronger flares affect larger areas in the photosphere, which is in agreement with pre-

vious studies (Petrie & Sudol 2010; Castellanos Durán et al. 2018). However, the change duration is only moderately related to the GOES X-ray flux.

Although the characteristics of field change such as ΔB_h , τ , the rate of field change ($\Delta B_h/\tau$) show weak or no relation with the active region area, they are very strongly related to the flare parameters (ribbon magnetic flux and flare ribbon area). The flare duration, τ_{GOES} , is positively correlated with the $S_{r_{bn}}$, $\Phi_{r_{bn}}$, and the class of flares (GOES X-ray peak flux, $cc=0.7$). From the analysis of 2956 flares, Reep & Knizhnik (2019) reported that in smaller flares the flare duration, defined as FWHM of the GOES X-ray light curve (τ_{FWHM}), is not correlated with the ribbon area, $S_{r_{bn}}$ ($cc=0.2$, C-class). On the other hand, they found that the correlation increases for larger M- and X-class flares: $cc=0.6$ (M-class) and $cc=0.9$ (X-class). In a different study, Toriumi et al. (2017) analyzed 51 large flares ($\geq M5.0$ -class), finding that the τ_{FWHM} is linearly correlated with $S_{r_{bn}}$, $\Phi_{r_{bn}}$, and ribbon separation, in agreement with our study.

According to the standard flare model the ribbon separation, $d_{r_{bn}}$, generally refers to the footpoint separation of flare loops. If we assume that the flare loops are semi-circular in shape then the $d_{r_{bn}}$ is proportional to the height of the reconnecting loops and loop length. We find that τ_{GOES} is moderately correlated with $d_{r_{bn}}$ ($cc=0.5$). From analysis of stronger-flares sample of flare class M5.0 and above, Toriumi et al. (2017) found that the reconnection timescale is proportional to the loop length with a slightly higher correlation coefficient ($\propto d_{r_{bn}}$, $cc=0.8$). Consequently, longer $d_{r_{bn}}$ value would give rise to longer flare duration, which is similar to our result (see Figure 9k). Using hydrodynamic modeling Reep & Toriumi (2017) also found a clear linear correlation between the ribbon separations and the FWHM of GOES light curves, indicating that the primary factors that control large-flare timescale are reconnection duration and the loop length.

The field change rate, $\Delta B_h/\tau$, is inversely proportional to the ribbon separation $d_{r_{bn}}$ (Figure 9l) and the GOES flare duration τ_{GOES} (Figure 9l). Events having shorter τ value and smaller loop size exhibit faster field change. This relation suggests that a low-lying loop or smaller $d_{r_{bn}}$, that is moderately correlated with τ , would result in a fast $\Delta B_h/\tau$. In our data set the median value of field change duration, τ , ranges from 5 to 17.5 minutes, where stronger flares exhibit longer τ .

Finally, the scatter plot between τ and τ_{GOES} , which is defined as the time difference between GOES flare start and end time, shows remarkably strong linear relation with a Spearman correlation coefficient value of

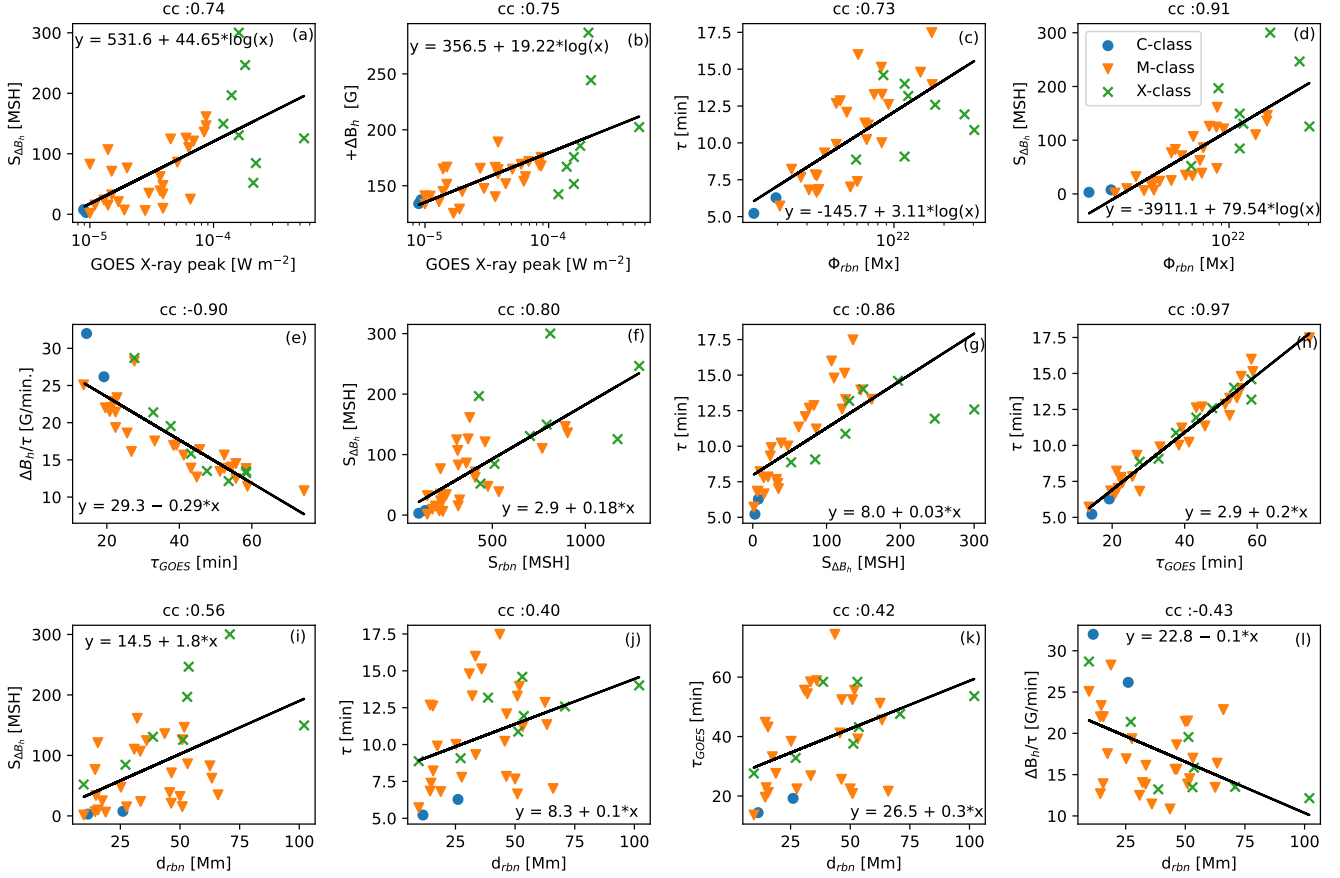


Figure 9. Statistical properties of horizontal field changes during 37 flares. Scatter plots showing relation between (a) GOES X-ray flux vs total area showing permanent change ($S_{\Delta B_h}$), (b) GOES X-ray flux vs positive permanent change in B_h ($+\Delta B_h$), (c) total ribbon flux (Φ_{rbn}) vs field change duration (τ), (d) Φ_{rbn} vs Area ΔB_h , (e) GOES flare duration (τ_{GOES}) vs rate of field change ($\Delta B_h/\tau$), (f) total area of ribbons (A_{rbn}) vs Area ΔB_h , (g) Area ΔB_h vs τ , (h) τ_{GOES} vs τ , (i) ribbon distance (d_{rbn}) vs Area ΔB_h , (j) d_{rbn} vs τ , (k) d_{rbn} vs τ_{GOES} , and (l) d_{rbn} vs $\Delta B_h/\tau$. In the top panel the abscissa is in log scale. A solid line refers to the linear fit between parameters. In each plot, ‘cc’ corresponds to the Spearman correlation coefficient value. The filled circle, triangle, and cross symbols correspond to C-, M-, and X-class flares, respectively. Gray vertical lines refer to the standard deviation of parameters. The Area is expressed in millionths of the solar hemisphere (MSH), which is equivalent to $3 \times 10^6 \text{ km}^2$.

0.97. We find that the permanent field change duration ranges from 23% to 42% of the total flaring duration, with an average value of 29%.

4. DISCUSSION

We present statistical analysis of magnetic field changes associated with 37 flares. We investigate how the photospheric magnetic field vector changes using high-cadence vector magnetograms obtained from the HMI/SDO. We also examine how the characteristics of the field change are associated with the ribbon morphology and the UV emission. Although there are different types of field changes in the B_h and B_z , we focus on the step-like and permanent changes in B_h . The characteristics of field change are obtained by fitting a time series of each pixel by a step-like function.

The increase of B_h or increase in field inclination in all events, mainly near the PIL, is in agreement with previous studies (Sun et al. 2017; Petrie 2019; Liu et al. 2022). The high-resolution vector magnetograms from HMI/SDO allowed us to investigate the fast permanent field changes ($>135 \text{ s}$). Nevertheless we find pixels showing permanent changes on faster time scales than the cadence of our data set. It suggests that further high-cadence observations are needed to explore the relation of fast photospheric changes with flares. We also noticed that the permanent field change or step-like change is also evident in the temporal evolution of B_z , but these changes are scarcely distributed over the FOV compared to the B_h . Due to lack of statistics, we did not analyze B_z change in detail.

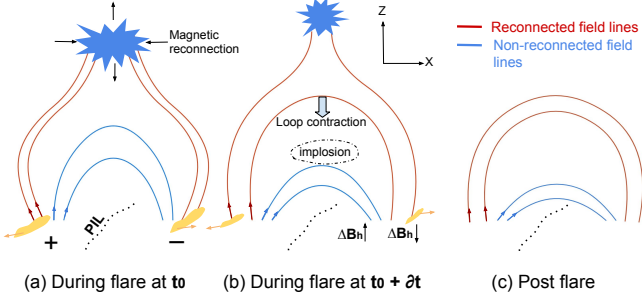


Figure 10. A sketch of the magnetic field configuration (a, b) during and (c) after a flaring time. Solid lines refer to the field lines connecting opposite polarities, which are indicated by ‘+’ and ‘-’ signs. A dotted line refers to the polarity inversion line (PIL), whereas the ribbons are shown with a yellow-colored area near the footpoints. Blue field lines contract due to coronal implosion whereas the newly reconnected field lines shown in red shrink after reconnection. Here, the ‘Z’ axis is perpendicular to the solar surface, whereas ‘X’ is along the solar surface.

It is well known that a flare can occur anywhere in the upper atmosphere. If a loop is considered to be a semicircular shape then the ribbon distance, d_{rbn} , would be proportional to loop length and the reconnection height (Toriumi et al. 2017). Consequently, a smaller d_{rbn} would correspond to larger energy release in the lower atmosphere where fields are stronger, whereas a larger d_{rbn} (longer loops) would correspond to smaller energy release in the higher layers of the solar atmosphere. Based on above assumptions, we can speculate that a flare with smaller d_{rbn} would release energy in the deeper layers of the solar atmosphere and lead to larger and faster magnetic field changes. Recently, Liu et al. (2022) reported that the initial ribbon separation is roughly inversely proportional to the mean value of B_h change in 35 solar flares (21 X- and 14 $> M6$ -class flares), especially for smaller distances ($cc=0.4$). In contrast, using a much weaker flare sample of 8 X-, 7 $> M6$ and 22 $< M6$ flares, here we find that magnitude of positive B_h change shows no correlation with the ribbon distance ($cc = 0.03$). This difference could be due to e.g. our different approach to estimate the ribbon separation or a different physical process at play for weaker flares that we analyze here.

Figures 8 & 9 illustrate that the area affected by a flare or pixels exhibiting permanent change in horizontal field, $S_{\Delta B_h}$, is not only strongly correlated with d_{rbn} ($cc = 0.6$, Panel i) but also strongly correlated with the Φ_{rbn} ($cc = 0.91$, Panel d), S_{rbn} ($cc = 0.8$, Panel f), $I_{X,\text{peak}}$ ($cc = 0.74$) and τ_{GOES} ($cc = 0.85$). We can speculate that a stronger flare, having larger S_{rbn} , Φ_{rbn} , and τ_{GOES} , would give rise to longer reconnection pro-

cesses, and thus affect more pixels with a longer field change duration. Consequently, a stronger flare with larger ribbon area and magnetic flux can penetrate and affect the deeper layers, resulting in an increase in B_h mainly near the PIL. Furthermore, no clear relation between the d_{rbn} and the magnitude of field change ΔB_h ($cc=0.06$) suggests that the magnetic field change in the photosphere is not related to the reconnection heights but depends strongly on the S_{rbn} ($cc = 0.61$), Φ_{rbn} ($cc = 0.63$), and $I_{X,\text{peak}}$ ($cc = 0.75$).

The observed increase of B_h can be related to the coronal implosion conjecture, where the coronal field lines contract after releasing stored magnetic field energy (Hudson 2000). In this conjecture, the loop contraction arises due to decrease in magnetic pressure and volume reduction at the reconnection sites. Moreover, the velocity disturbances generated at the flare site could also be responsible for loop contraction without being reconnected (Zuccarello et al. 2017; Sarkar et al. 2017). Additionally, B_h increase could be a result of the reconnection-driven contraction of sheared flare loops, as has been recently demonstrated by Barczynski et al. (2019) using 3D magnetohydrodynamic simulation. During magnetic reconnection, magnetic field lines of opposite direction break and then reconnect, forming newly reconnected field lines that contract and accelerate plasma away from the reconnection site (Longcope et al. 2009). The newly formed field lines contract towards the deeper layers to attain a stable configuration or relax to a quasi-force-free state.

We suggest that the above mentioned mechanisms can all contribute to the observed change in B_h during flares. A possible scenario demonstrating how the magnetic field structure changes during a flare is shown in Figure 10. The sketch depicts that the inner loops lying between yellow flare ribbons might become more horizontal due to loop contraction caused by the magnetic implosion or velocity disturbances (Sarkar et al. 2017), whereas the field lines closer to outer loops and within the flare ribbons might become more vertical from contracting reconnected loops due to rearrangement of post-reconnection field lines following magnetic reconnection. We would like to note though that there is a large variation in the relationship between ribbons morphology and locations of horizontal field increases, indicating that the field change is a result of both processes.

We also investigated how the permanent field change in the photosphere is associated with the UV emission. We find that not all pixels showing permanent field change in B_h are associated with the UV emission (AIA 1600 Å intensity enhancement). For all events, the percentage of pixels showing both AIA 1600 Å intensity

enhancement and permanent field change range from 4 to 50%. As the magnetic field measurements in our data have higher noise, small changes (< 100 G) in $B_{h,z}$ associated with ribbons are not analyzed in this study.

We also investigated how the field change start time is related to the UV emission start time for the pixels showing both UV and permanent B_h change. In 31 events out of a total 37, we find that the UV emission starts early compared to the field change start time, where the median and maximum delay is 4.4 and 19 minutes, respectively. This relation suggests that the majority of magnetic field changes in the photosphere are consequences of flares. From the analysis of four X-class solar flares [Johnstone et al. \(2012\)](#) reported that the UV emissions preceded the photospheric field changes by 4 minutes on average with the longest lead being 9 minutes, which is in agreement with our findings.

On the other hand, six events show early (a few minutes) field changes compared to UV emission. The reason for this early change is not clear. One of the possibilities to explain this could be the magnetic reconnection at deeper layers, whereas the UV emission would be a result of reconnection at higher layers or delayed particle acceleration. Recently, [Burtseva et al. \(2015\)](#) studied the correlation between abrupt permanent changes of magnetic field and hard X-ray emission observed by RHESSI during six X-class flares. They also reported that amplitudes of the field changes peak a few minutes earlier than the peak of the hard X-ray signal.

Why do the chromosphere brightenings show early rise compared to the field changes in the photosphere? This could be related to the energy deposition by MHD or Alfvén waves generated by sudden change in the field lines in the corona, though the real reason is not yet clear. These waves travel in all directions including the lower solar atmosphere and can take a few minutes to reach the bottom of corona ([Hudson et al. 2008](#)). The release of energy through interaction of waves with the dense chromospheric plasma, gives rise to chromospheric brightenings ([Emslie & Sturrock 1982](#); [De Pontieu et al. 2001](#); [Fletcher & Hudson 2008](#)). Consequently, we see chromospheric brightening first compared to the field changes in the photosphere.

We also find a remarkable positive correlation ($cc = 0.97$) between τ_{GOES} and τ . This implies that a flare having longer duration will result in longer field change duration, irrespective of flare intensity. Although there are different types of field changes during a flare, on average 29% of the total flare duration time exhibit permanent field changes.

In this study we focused on the permanent step-like change, however, there are different types of changes oc-

curing in the photosphere at different locations. One of our future studies will include investigation of all kinds of field changes and their preferred locations not only in the photosphere but also in the chromosphere. Machine-learning algorithms would be useful to classify and identify different complex types of field changes occurring during a flare and thus could improve our understanding of magnetic imprints of flares in the lower solar atmosphere.

5. CONCLUSION

In this paper we have utilized high-cadence vector magnetograms observed by HMI/SDO to investigate magnetic imprints in the photosphere during 37 flares, mostly M- and X-class, and their association with the ribbon morphology. Our main findings are shown in Figures 8 & 9 and are highlighted below.

1. In all events the pixels showing permanent and step-like change in the horizontal B_h and vertical B_z components of the magnetic field are distributed all over the AR, but the majority of them are located close to the PIL for B_h . Pixels showing changes in B_z are less pronounced and are distributed in small patches over the whole AR. In all cases, the magnitude of field change in B_h is stronger than in B_z .
2. We find that pixels located near the PIL exhibit early field change and shorter change duration with larger magnitudes of field change ΔB_h compared to pixels located $\sim 10''$ away from the PIL.
3. We find no clear relation between the temporal evolution of vertical current density J_z and B_h field components for the pixels exhibiting permanent and step-like changes. Some pixels near the PIL show step-like changes in J_z but they are not consistent with the permanent magnetic field changes.
4. We find that not all pixels showing permanent field change in B_h are associated with the UV emission or vice-versa. For all events, the percentage of pixels showing both AIA 1600 Å intensity enhancement and permanent field change range from 4 to 50% of all pixels in the selected regions. In 31 events out of a total 37, we find that the UV emission starts early compared to field change start time, with the median and maximum delays of around 4.4 and 19 minutes, respectively.
5. The median magnetic field change magnitude ΔB_h for all events ranges from 100 G to 300 G. We find

that the total area showing permanent change in B_h and the magnitude of ΔB_h are strongly correlated with the GOES peak X-ray flux.

6. The characteristics of field change such as magnitude of permanent field change (ΔB_h), field change duration (τ), the rate of field change ($\Delta B_h/\tau$) show weak or no relation with the active region area, but are very strongly related to the flare parameters (Φ_{rbn} , S_{rbn} , τ_{GOES}).
7. The permanent field change duration, τ , is strongly correlated with the GOES flare duration (τ_{GOES} ; $cc = 0.97$). We find that this permanent field change duration ranges from 23% to 42% of τ_{GOES} , with an average value of 29%. The median value of field change ranges from 5 to 17.5 minutes, with τ_{GOES} ranging from 14 to 74 minutes.
8. Finally, we find that the total area showing permanent change ($S_{\Delta B_h}$), field change duration (τ), and the GOES flare duration (τ_{GOES}) are positively correlated with the ribbon distance (d_{rbn}), whereas the magnitude of field change is not correlated with d_{rbn} .

In Figure 10 we summarize the results of our analysis where magnetic field changes in the horizontal and vertical components in the photosphere are a consequence of magnetic reconnection and magnetic field implosion. As a result of this combination we observe an increase in B_h near the PIL and decrease in B_h away from the PIL. A real configuration of magnetic field lines during a flare can be more complex at different heights. Therefore, to present a clear picture we need multi-height spectropolarimetric observations, especially in the lower solar atmosphere (e.g. the Daniel K. Inoue Solar Telescope, DKIST, Rast et al. 2020).

We thank the HMI team for providing us with the vector magnetic field SDO/HMI data and the AIA team for providing us with the SDO/AIA data. We acknowledge support from NASA LWS NNH17ZDA001N, NASA LWS 80NSSC19K0070, NASA ECIP 80NSSC19K0910 and NSF CAREER award SPVKK1RC2MZ3 (R.Y. and M.D.K.) This research has made use of NASA's Astrophysics Data System. We acknowledge the community effort devoted to the development of the following open-source packages that were used in this work: numpy (numpy.org), matplotlib (matplotlib.org) and SunPy (sunpy.org).

REFERENCES

- Balasubramaniam, K. S., Pevtsov, A. A., Neidig, D. F., et al. 2005, *ApJ*, 630, 1160
- Barczynski, K., Aulanier, G., Masson, S., & Wheatland, M. S. 2019, *ApJ*, 877, 67
- Benz, A. O. 2008, *Living Reviews in Solar Physics*, 5, 1
- Borrero, J. M., Tomczyk, S., Kubo, M., et al. 2011, *SoPh*, 273, 267
- Burtseva, O., Martínez-Oliveros, J. C., Petrie, G. J. D., & Pevtsov, A. A. 2015, *ApJ*, 806, 173
- Carmichael, H. 1964, *NASA Special Publication*, Vol. 50, 451
- Castellanos Durán, J. S., Kleint, L., & Calvo-Mozo, B. 2018, *ApJ*, 852, 25
- De Pontieu, B., Martens, P. C. H., & Hudson, H. S. 2001, *ApJ*, 558, 859
- Emslie, A. G., & Sturrock, P. A. 1982, *SoPh*, 80, 99
- Fisher, G. H., Bercik, D. J., Welsch, B. T., & Hudson, H. S. 2012, *SoPh*, 277, 59
- Fletcher, L., & Hudson, H. S. 2008, *ApJ*, 675, 1645
- Gary, G. A., & Hagyard, M. J. 1990, *SoPh*, 126, 21
- Gosain, S. 2012, *ApJ*, 749, 85
- Hagenaar, H. J., & Shine, R. A. 2005, *ApJ*, 635, 659
- Hirayama, T. 1974, *SoPh*, 34, 323
- Hudson, H. S. 2000, *ApJL*, 531, L75
- . 2011, *SSRv*, 158, 5
- Hudson, H. S., Fisher, G. H., & Welsch, B. T. 2008, in *Astronomical Society of the Pacific Conference Series*, Vol. 383, *Subsurface and Atmospheric Influences on Solar Activity*, ed. R. Howe, R. W. Komm, K. S. Balasubramaniam, & G. J. D. Petrie, 221
- Johnstone, B. M., Petrie, G. J. D., & Sudol, J. J. 2012, *ApJ*, 760, 29
- Kazachenko, M. D., Albelo-Corchado, M. F., Tamburri, C. A., & Welsch, B. T. 2022a, *SoPh*, 297, 59
- Kazachenko, M. D., Canfield, R. C., Longcope, D. W., & Qiu, J. 2012, *SoPh*, 277, 165
- Kazachenko, M. D., Lynch, B. J., Savcheva, A., Sun, X., & Welsch, B. T. 2022b, *ApJ*, 926, 56
- Kazachenko, M. D., Lynch, B. J., Welsch, B. T., & Sun, X. 2017, *ApJ*, 845, 49
- Kleint, L. 2017, *ApJ*, 834, 26
- Kopp, R. A., & Pneuman, G. W. 1976, *SoPh*, 50, 85
- Lemen, J. R., Title, A. M., Akin, D. J., et al. 2012, *SoPh*, 275, 17

- Li, Y., Jing, J., Fan, Y., & Wang, H. 2011, *ApJL*, 727, L19
- Liu, C., Xu, Y., Cao, W., et al. 2016, *Nature Communications*, 7, 13104
- Liu, L., Zhou, Z., Wang, Y., Sun, X., & Wang, G. 2022, *ApJL*, 934, L33
- Liu, R., Wang, H., & Alexander, D. 2009, *ApJ*, 696, 121
- Longcope, D., Beveridge, C., Qiu, J., et al. 2007, *SoPh*, 244, 45
- Longcope, D. W., Guidoni, S. E., & Linton, M. G. 2009, *ApJL*, 690, L18
- Maurya, R. A., Vemareddy, P., & Ambastha, A. 2012, *ApJ*, 747, 134
- Pesnell, W. D., Thompson, B. J., & Chamberlin, P. C. 2012, *SoPh*, 275, 3
- Petrie, G. J. D. 2012, *ApJ*, 759, 50
- Petrie, G. J. D. 2019, *ApJS*, 240, 11
- Petrie, G. J. D., & Sudol, J. J. 2010, *ApJ*, 724, 1218
- Pettauer, T., & Brandt, P. N. 1997, *SoPh*, 175, 197
- Qiu, J., Longcope, D. W., Cassak, P. A., & Priest, E. R. 2017, *ApJ*, 838, 17
- Rast, M. P., Bello González, N., Bellot Rubio, L., et al. 2020, *arXiv e-prints*, arXiv:2008.08203
- Reep, J. W., & Knizhnik, K. J. 2019, *ApJ*, 874, 157
- Reep, J. W., & Toriumi, S. 2017, *ApJ*, 851, 4
- Russell, A. J. B., Simões, P. J. A., & Fletcher, L. 2015, *A&A*, 581, A8
- Sarkar, A., Vaidya, B., Hazra, S., & Bhattacharyya, J. 2017, *ApJ*, 851, 120
- Scherrer, P. H., Schou, J., Bush, R. I., et al. 2012, *SoPh*, 275, 207
- Schrijver, C. J. 2015, *Space Weather*, 13, 524
- Simões, P. J. A., Fletcher, L., Hudson, H. S., & Russell, A. J. B. 2013, *ApJ*, 777, 152
- Sturrock, P. A. 1966, *Nature*, 211, 695
- Sudol, J. J., & Harvey, J. W. 2005, *ApJ*, 635, 647
- Sun, X., Hoeksema, J. T., Liu, Y., Kazachenko, M., & Chen, R. 2017, *ApJ*, 839, 67
- Toriumi, S., Schrijver, C. J., Harra, L. K., Hudson, H., & Nagashima, K. 2017, *ApJ*, 834, 56
- Wang, J., Simões, P. J. A., Fletcher, L., et al. 2016, *ApJ*, 833, 221
- Wang, S., Liu, C., Deng, N., & Wang, H. 2014, *ApJL*, 782, L31
- Wang, S., Liu, C., Liu, R., et al. 2012, *ApJL*, 745, L17
- Xu, Y., Cao, W., Ahn, K., et al. 2018, *Nature Communications*, 9, 46
- Yadav, R., Díaz Baso, C. J., de la Cruz Rodríguez, J., Calvo, F., & Morosin, R. 2021, *A&A*, 649, A106
- Zuccarello, F. P., Aulanier, G., Dudík, J., et al. 2017, *ApJ*, 837, 115

APPENDIX

Table 2. List of B_h change properties for 37 flares (see Table 1). For each event the median value of the following parameters is listed: total area showing step-like change ($S_{\Delta B_h}$), positive and negative change in B_h , mid-time of field change (T_m) since flare start time, field change duration (τ), field change start time (T_s) since flare start time, and field change rate ($\Delta B_h/\tau$). The area is expressed in millionths of the solar hemisphere (MSH), which is equivalent to 3×10^6 km².

Event no.	Flare start time (UT)	Flare Class	$S_{\Delta B_h}$ (MSH)	$+\Delta B_h$ (G)	$-\Delta B_h$ (G)	T_m (min.)	τ (min.)	T_s (min.)	$ \Delta B_h /\tau$ (G/min.)
1	2010-08-07T17:55	M1.0	82.8	141.0 \pm 74.5	159.3 \pm 92.7	24.4	12.9	14.7	13.5
2	2011-02-15T01:43	X2.2	84.6	244.3 \pm 146.2	153.1 \pm 103.4	14.3	9.1	8.1	21.4
3	2011-08-03T13:17	M6.0	125.9	169.2 \pm 119.9	162.5 \pm 105.0	25.2	13.3	15.6	13.9
4	2011-09-06T22:11	X2.1	52.0	286.9 \pm 178.8	170.9 \pm 120.7	10.6	8.9	5.5	28.7
5	2011-10-02T00:37	M3.9	9.8	164.5 \pm 108.9	147.7 \pm 74.5	10.8	8.2	5.4	22.0
6	2011-11-15T12:29	M1.9	7.0	129.1 \pm 114.9	138.7 \pm 116.9	10.7	6.8	6.5	22.0
7	2011-12-27T04:11	C8.9	7.6	134.0 \pm 84.3	158.1 \pm 89.7	9.9	6.3	5.9	26.2
8	2012-01-23T03:37	M8.7	146.3	175.3 \pm 118.2	180.7 \pm 123.8	27.2	14.0	17.4	14.5
9	2012-03-07T00:01	X5.4	125.6	202.4 \pm 148.9	165.9 \pm 121.9	16.3	10.9	9.2	19.6
10	2012-03-09T03:21	M6.3	110.2	154.0 \pm 120.1	168.2 \pm 122.5	25.1	14.8	14.9	12.5
11	2012-03-10T17:15	M8.4	135.9	168.5 \pm 118.7	157.7 \pm 124.7	33.4	17.5	22.3	10.8
12	2012-03-14T15:07	M2.8	6.1	165.6 \pm 109.1	177.1 \pm 119.3	14.3	6.8	9.4	28.3
13	2012-07-12T15:37	X1.4	196.8	167.0 \pm 121.4	180.7 \pm 129.4	30.1	14.6	20.7	13.5
14	2012-11-21T06:45	M1.4	14.9	144.9 \pm 110.0	143.2 \pm 93.4	11.3	7.8	6.1	19.3
15	2013-04-11T06:55	M6.5	25.0	158.1 \pm 115.6	150.9 \pm 108.5	16.6	9.9	8.8	17.5
16	2013-05-16T21:35	M1.3	23.7	135.8 \pm 82.7	140.9 \pm 96.7	13.8	9.3	8.2	16.1
17	2013-05-31T19:51	M1.0	1.5	133.9 \pm 65.7	152.1 \pm 94.3	7.3	5.7	4.5	25.1
18	2013-08-17T18:49	M1.4	106.8	165.0 \pm 128.4	195.8 \pm 134.3	28.5	16.0	17.8	13.8
19	2013-12-28T17:53	C9.3	3.0	137.5 \pm 104.5	193.5 \pm 82.2	7.7	5.2	5.0	32.0
20	2014-01-07T18:03	X1.2	149.6	142.4 \pm 86.0	146.0 \pm 96.6	25.4	14.0	15.9	12.2
21	2014-01-31T15:31	M1.1	15.3	140.7 \pm 76.7	142.2 \pm 92.6	10.2	6.7	5.8	21.5
22	2014-02-01T07:13	M3.0	34.8	147.5 \pm 114.0	139.5 \pm 88.8	10.0	7.0	5.5	22.9
23	2014-02-12T03:51	M3.7	62.3	166.5 \pm 129.1	159.2 \pm 123.1	22.7	11.3	14.3	16.4
24	2014-03-20T03:41	M1.7	20.8	125.3 \pm 79.3	137.1 \pm 95.9	11.9	7.8	6.2	18.6
25	2014-08-01T17:55	M1.5	71.1	166.6 \pm 112.5	168.0 \pm 118.2	23.1	12.1	14.3	15.7
26	2014-08-25T14:45	M2.0	76.6	144.8 \pm 129.1	142.6 \pm 85.2	21.1	12.7	12.2	12.7
27	2014-08-25T20:05	M3.9	33.7	189.1 \pm 108.4	144.8 \pm 63.8	10.7	7.4	5.7	23.4
28	2014-09-08T23:11	M4.5	124.4	151.8 \pm 102.9	158.3 \pm 109.2	31.6	15.1	21.4	11.4
29	2014-09-10T17:21	X1.6	130.8	175.7 \pm 92.0	145.8 \pm 91.2	25.6	13.2	15.6	13.2
30	2014-09-28T02:39	M5.1	86.0	164.8 \pm 121.2	167.2 \pm 118.8	18.2	11.2	10.5	17.0
31	2014-10-22T14:01	X1.6	300.2	151.6 \pm 120.5	152.6 \pm 113.4	24.0	12.6	15.2	13.5
32	2014-12-17T00:57	M1.5	32.1	151.3 \pm 109.9	151.6 \pm 108.1	11.0	7.7	6.3	21.4
33	2014-12-17T04:25	M8.7	161.2	167.7 \pm 114.7	165.0 \pm 130.8	25.7	13.3	14.9	14.0
34	2014-12-18T21:41	M6.9	121.0	171.6 \pm 92.7	145.1 \pm 105.8	22.3	12.6	14.0	13.9
35	2014-12-20T00:11	X1.8	246.6	185.7 \pm 113.4	164.1 \pm 109.2	18.6	11.9	10.8	15.8
36	2015-11-04T13:31	M3.7	38.5	140.2 \pm 77.1	148.7 \pm 72.2	19.7	10.2	12.8	15.6
37	2015-11-09T12:49	M3.9	47.4	160.7 \pm 87.0	159.7 \pm 103.3	17.5	10.0	10.2	16.9

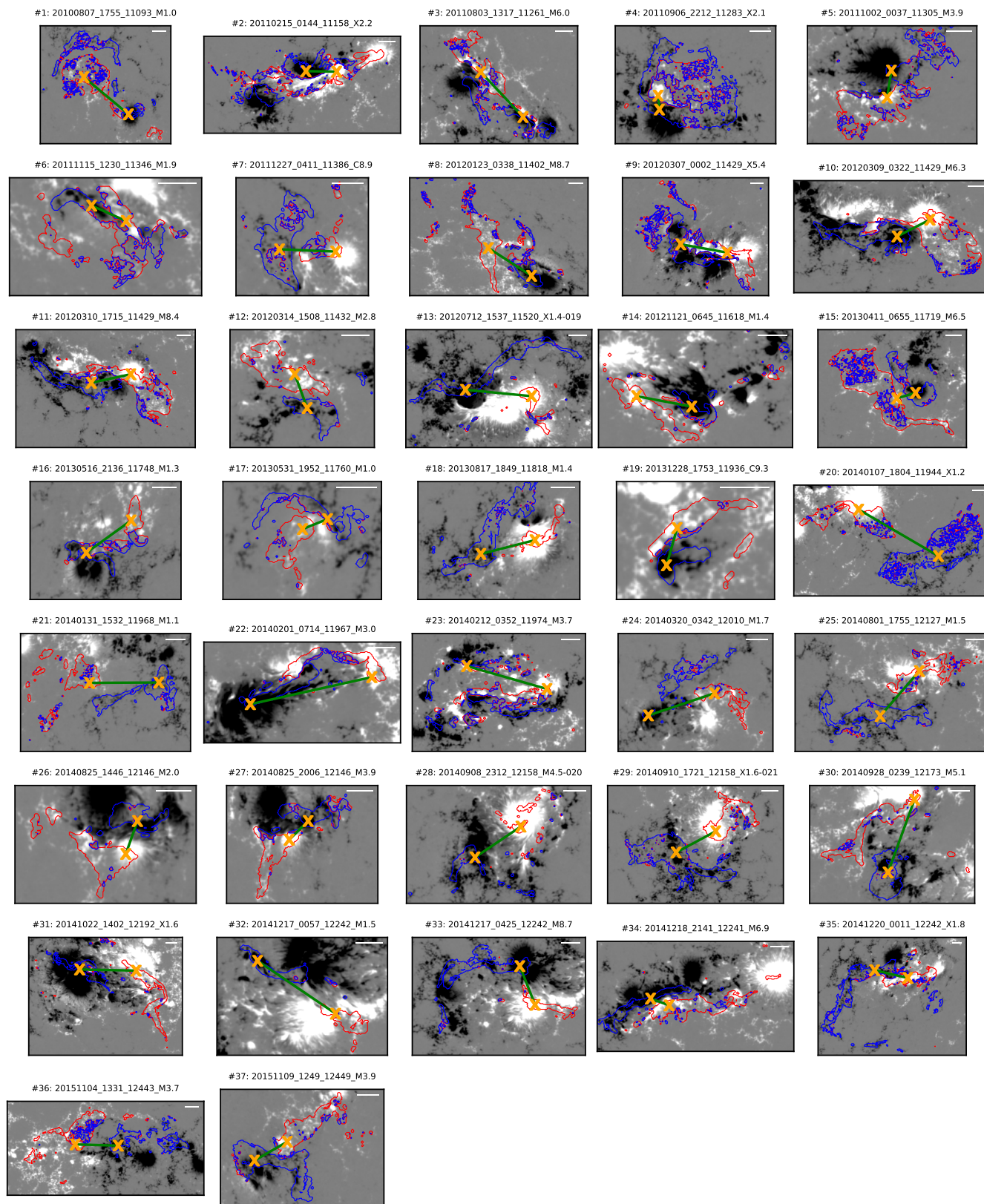


Figure 11. Overview of cumulative ribbons in 37 analyzed flares. The background image shows the B_z component of the magnetic field, where black and white indicate negative and positive polarities (saturated at ± 800 G), respectively. Red and blue contours refer to the cumulative ribbons over the positive and negative polarities of B_z , respectively. The magnetic-flux weighted centroids of the ribbons are indicated by cross signs, which are connected by a solid green line. A solid horizontal white line in each panel indicates the length of $20''$. The flare index is highlighted in the title of each panel.

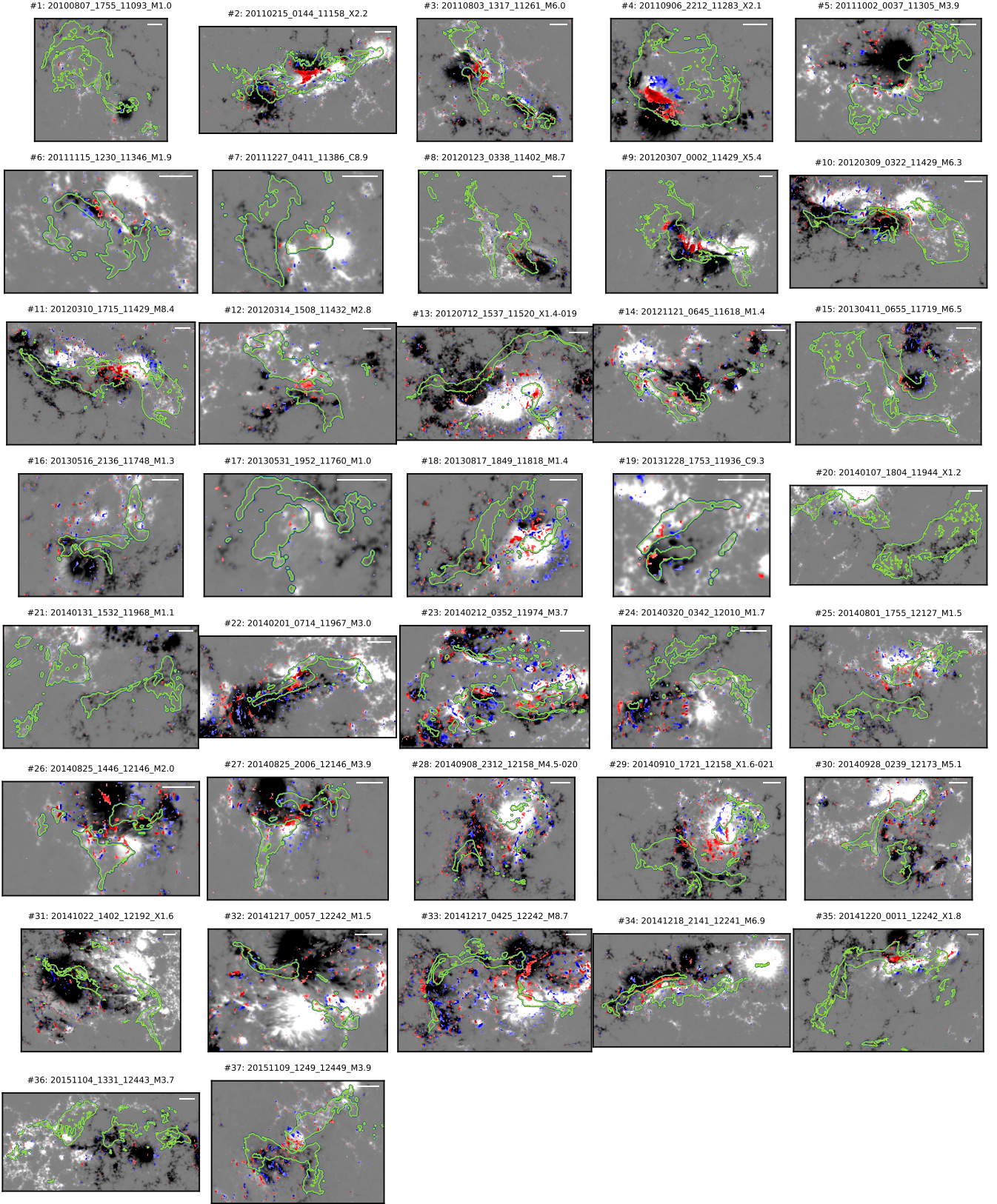


Figure 12. Overview of horizontal magnetic field changes in 37 analyzed flares. Each panel shows the difference in B_h at flare start and end times, $\Delta B_h = B_h(T_e) - B_h(T_s)$, where blue and red colors represent negative and positive changes (saturated at ± 600 G). The background image shows the B_z component of the magnetic field, where black and white indicate negative and positive polarities (saturated at ± 800 G), respectively. The green contours refer to the cumulative flare ribbons. A solid horizontal white line in each panel indicates the length of $20''$.